Novel Nb^{5+}-doped hexagonal perovskite Ba$_5$In$_2$Al$_2$ZrO$_{13}$ (structure, hydration, electrical conductivity)

Roman D. Andreev [ab] , Daniil V. Korona [ab] , Irina A. Anokhina [ab] ,
Irina E. Animitsa [ab] *

a: Institute of Natural Sciences, Ural Federal University, Yekaterinburg 620009, Russia
b: Institute of High Temperature Electrochemistry of the Ural Branch of the Russian Academy of Sciences, Yekaterinburg 620990, Russia
* Corresponding author: irina.animitsa@urfu.ru

This paper belongs to a Regular Issue.

Abstract

A new phase Ba$_5$In$_2$Al$_2$Zr$_{0.9}$Nb$_{0.1}$O$_{13.05}$ with a hexagonal perovskite structure was obtained. The substitution of Zr^{4+} by smaller Nb^{5+} was accompanied by the incorporation of the oxygen interstitials and did not lead to a significant change in the lattice parameters. It was established that the investigated sample was capable of water incorporation from the gas phase; the hydration degree value was 0.24 mol H$_2$O. IR-spectroscopy analysis revealed the presence of OH$^-$-groups with different thermal stability, which participate in different hydrogen bonds. The new phase Ba$_5$In$_2$Al$_2$Zr$_{0.9}$Nb$_{0.1}$O$_{13.05}$ demonstrates the predominant protonic conductivity at pH$_2$O = 2·10^{-2} atm and T < 600 °C.

1. Introduction

Searching for novel functional materials represents an important direction in the research and development of alternative energy sources. On the way to solving this problem, such a class of materials as perovskites has attracted much attention [1–3]. Due to their unique structural and compositional flexibility and high stability, perovskite oxides and their derivatives are still being extensively studied. This made it possible to obtain a wide variety of new compounds with a variable set of properties [4–6].

Some directions towards modifying the composition and structure of perovskites can be distinguished. Doping the ABO$_3$ perovskite materials at A-, B- and O-sites does not change the perovskite structure can induce defects in the resulting materials, such as, most commonly, oxygen vacancies. The oxygen vacancies can be introduced by substituting A- and B-site cations with the cations of lower valence. In recent years, the defect-perovskite materials have been explored to enhance their electrical and catalytic properties [7].

Another modification strategy is the formation of several sublattices, for example, the compositions AA´B$_2$O$_6$ or A$_2$BB´O$_6$. The double perovskite structure is so named because the unit cell is twice that of the perovskite. It has the same architecture of 12-coordinated A sites and 6-coordinated B sites, but two cations are ordered on the A- or B-sites. The B-site can either be ordered or disordered, generally as a result of charge or size of the cations. When the size or charge are similar then B/B′ cations are disordered and randomly distributed throughout the perovskite network. If the mismatch between size and charge becomes large, the B-sites order in a 1:1 checkerboard fashion known as rock salt ordering, and the structure is now called a double perovskite [8]. Such compounds can also be oxygen-deficient, considering the corresponding oxidation states of the elements [9]. Among such phases, many oxygen-ion and proton conductors are known [10–12]. There are also perovskites where the A-sites and B-sites can order simultaneously. This results in a structure called a doubly ordered double perovskite with the general formula AA'BB'O$_6$. The type of B-site ordering is very commonly observed, but A-site ordering is much less commonly observed and has specific structural requirements.

More complex structures are layered perovskites, for example, Ruddlesden-Popper (RP), Aurivillius and Dion-Jacobson (DJ) phases [13–16]. Layered perovskites consist of infinite 2D slabs of the ABO$_3$ type structure which are separated by some motif. The general formula for the layers is A$_{n-1}$B$_n$O$_{3n+1}$. Dion-Jacobson phases, with the general formula $A'A_{n-1}B_nX_{3n+1}$, are similar to RP phases but have one less A' cation in the interlayer. Both RP and DJ phases form homologous series with variable numbers of perovskite layers.

Even more complex types of structures are intergrowth structures. In such structures, the perovskite block can be spliced with another structurally related block. Among such structures, new classes of oxygen-ion and proton conductors have recently been discovered [17, 18]. The hexagonal perovskite with the composition of $Ba_5Er_2Al_2ZrO_{13}$ exhibited high proton conductivity 10^{-3} S·cm^{-1} at 300 °C as the best proton conductors based on doped barium cerates [19]. The structure of $Ba_5Er_2Al_2ZrO_{13}$ can be represented as an oxygen-deficient hexagonal perovskite derivative formed by an intergrowth of β-Ba_2ScAlO_5-type structural blocks and perovskite blocks [19]. Hydration of $Ba_5Er_2Al_2ZrO_{13}$ occurs within the intrinsically oxygen-vacant layers. This ability to hydrate is responsible for creating proton current carriers and the appearance of high-temperature proton conductivity.

Another hexagonal perovskite $Ba_5In_2Al_2ZrO_{13}$ has also recently been described as being capable of exhibiting proton transport [20]. The structure of this compound can be considered as a result of the intergrowth of oxygen-deficient Ba_2InAlO_5-blocks and $BaZrO_3$-blocks [21]. Acceptor doping of this phase by introduction of In^{3+} in the Zr^{4+}-sublattice was accompanied by some increase in proton conductivity [20], but the increase was small. In this regard, other types of doping, such as donor doping, may be of interest. Unlike in classical perovskites, the possibility of existence of interstitial oxygen in hexagonal perovskite has been proven [22]. Nevertheless, it remains unclear what types of dopants are appropriate in terms of optimizing ionic conductivity for such structures, because ionic conductors with hexagonal perovskite-related structures are quite rare and there are few works devoted to such studies.

In this study, the doped composition $Ba_5In_2Al_2Zr_{0.9}Nb_{0.1}O_{13.05}$ based on $Ba_5In_2Al_2ZrO_{13}$ phase was prepared by the solid-state method, and its conductivity as a function of T and pO_2 was investigated for the first time. The hydration processes, the nature of oxygen-hydrogen groups and proton transport were examined for the first time. The discussion of the obtained results was carried out in comparison with the previously obtained data for the phases $Ba_5In_2Al_2ZrO_{13}$ and $Ba_5In_{2.1}Al_2Zr_{0.9}O_{12.95}$ [20].

2. Experimental

Niobium doped hexagonal perovskite $Ba_5In_2Al_2Zr_{0.9}Nb_{0.1}O_{13.05}$ was synthesized through the solid-state route. Starting materials $BaCO_3$ (99.9999% purity, Vekton, RF), In_2O_3 (99.99% purity, Reachim, RF), Al_2O_3 (99.99% purity, Reachim, RF), ZrO_2 (99.99% purity, Reachim, RF) and Nb_2O_5 (99.99%, Reachim, RF) were preliminary dried, mixed together in stoichiometric ratio in agate mortar and ground for 1 h. Powder mixture was calcined at the temperature range of 800–1200 °C with increasing temperature for 100 °C at each step and intermediate grinding after each step. For the transport properties investigations, the ceramic samples were obtained by pressing powder into the pellets followed by sintering at 1400 °C for 24 h.

For the phase purity control, X-ray powder diffraction analysis was used. The measurements were carried out on an ARL EQUINOX 3000 (Thermo Fisher Scientific, Waltham, MA, USA) diffractometer at room temperature with Cu Kα radiation in the angle range of 10–90° with a step of 0.024°. For the cell parameters calculation FullProf software was used.

The surface morphology and cationic composition investigations were carried out on a VEGA3 (Tescan, Brno, Czech Republic) scanning electron microscope (SEM) equipped with the AztecLive Standard Ultim Max 40 (Oxford Instruments, Oxford, UK) system for energy dispersive X-ray spectroscopy (EDS).

The investigation of hydration process was made on a hydrated sample of $Ba_5In_2Al_2Zr_{0.9}Nb_{0.1}O_{13.95}$, prepared by cooling from 1100 °C to 200 °C under a flow of wet argon. Wet atmosphere for this experiment and further conductivity investigations was obtained by bubbling the gas (argon or air) through the saturated solution of potassium bromide KBr (pH_2O = 1.92·10^{-2} atm). The identification of hydrogen-oxygen groups in hydrated sample was made by using an infrared (IR) spectroscopy analysis. Investigations were performed with a Nicolet 6700 (Thermo Fisher Scientific, USA) FT-IR Spectrometer at room temperature.

Thermogravimetric (TG) measurements were performed on a Pyris 1 (PerkinElmer, Waltham, USA) TG analyzer. Firstly, the sample was heated at 1000 °C under a flow of dry argon, after that the sample was cooled to 25 °C with the rate of 1 °C per minute in the atmosphere of wet argon. The obtained TG-data were used for calculations of proton concentration. A mass-spectrum (MS) was obtained with quadrupole mass spectrometer QMS 403C Aëolos (Netzsch, Germany). The measurements were carried out in the temperature range of 25–1000 °C with the rate of 10 °C per minute in the atmosphere of dry argon.

For the transport properties investigations, the palladium-silver paste electrodes were painted on both sides of ceramic sample and fired for 3 h at 900 °C. Transport properties were studied by impedance spectroscopy technique using a Z-3000X (Elins, RF) frequency response analyzer (frequency range of 100 Hz – 3 MHz). The resistance values refinement was carried out using the Zview software. The measurements were performed in dry and wet atmospheres in the temperature range of 250–900 °C during cooling with the rate of 1 °C per min. Dry atmosphere was obtained by gas circulating through the phosphorous pentoxide powder P_2O_5 (pH_2O = 3.5·10^{-5} atm). The humidity of gases was measured using a humidity sensor HIH-3610 (Honeywell, USA). Conductivity was additionally investigated as a function of the oxygen partial pressure. The measurements were carried out under dry and wet atmospheres in oxygen partial pressure range of 10^{-18}–0.21 atm. The values of oxygen partial pressure were con-

trolled and measured by an electrochemical sensor and pump made of yttria-stabilized zirconia.

3. Results and Discussion

3.1. X-ray and morphological analysis

Figure 1 demonstrates X-ray diffraction patterns (XRD) of the powder Nb-doped phase $Ba_5In_2Al_2Zr_{0.9}Nb_{0.1}O_{13.05}$ in comparison with previously obtained undoped sample $Ba_5In_2Al_2ZrO_{13}$ and In-doped phase $Ba_5In_2Al_2Zr_{0.9}In_{0.1}O_{12.95}$ [20]. It is seen that all the diffractograms have a similar shape.

The investigated sample $Ba_5In_2Al_2Zr_{0.9}Nb_{0.1}O_{13.05}$ possess a primitive hexagonal structure similar to a parent compound $Ba_5In_2Al_2ZrO_{13}$, and can be characterized by the $P6_3/mmc$ space group.

The dissolving of niobium (V) oxide in the parent complex oxide matrix and solid solution formation can be described by the equation:

$$Nb_2O_5 \xrightarrow{ZrO_2} 2Nb^{\bullet}_{Zr} + 4O^x_O + O''_i \, , \qquad (1)$$
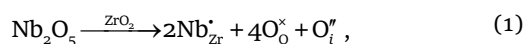
where $Nb^{\bullet}_{Zr}$ represents Nb^{5+} cation at a tetravalent Zr-site, O^x_O represents oxygen at a regular oxygen site and O''_i is an oxygen anion at an interstitial site. It can be seen from the diffractograms that diffraction peaks are slightly shifted toward high angles. This shift in angle values is attributed to the two factors: smaller ionic radii of niobium ($r_{Nb^{5+}}$ =0.64 Å [23]) in comparison with zirconium ($r_{Zr^{4+}}$ =0.72 Å [23]) and interstitial oxygen formation, that usually leads to unit cell expansion. The resulting change in lattice parameters was not significant. The lattice parameters for $Ba_5In_2Al_2Zr_{0.9}Nb_{0.1}O_{13.05}$, $Ba_5In_2Al_2ZrO_{13}$ and $Ba_5In_2Al_2Zr_{0.9}In_{0.1}O_{12.95}$ are presented in Table 1 in comparison. An example of Rietveld treatment for the X-ray diffraction data of the studied phase is presented in the Supplementary materials (Figure S1).
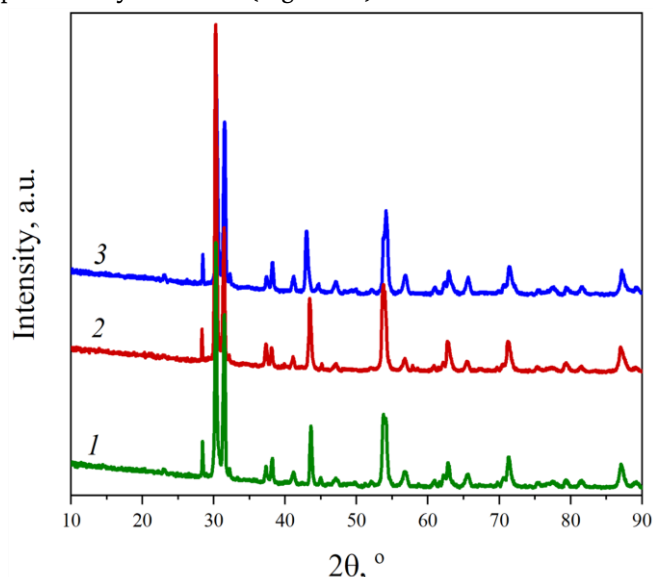
Figure 2 presents a SEM image of the ceramic sample $Ba_5In_2Al_2Zr_{0.9}Nb_{0.1}O_{13.05}$ and the results of EDS analysis. For the investigated sample the grains with the size of approximately 3–5 μm were observed; the grains with other sizes or composition were not observed. According to the results of EDS analysis, cation ratios obtained experimentally are in good agreement with the theoretical values. The experimental and theoretical values are shown in Table 2 in comparison.

3.2. IR spectroscopy investigations

IR spectra of undoped, In-doped and Nb-doped compounds are shown in Figure 3. All the spectra demonstrate similar shape. The presence of hydrogen-oxygen groups in hydrated phases is confirmed by a wide band in the range of 2500–3500 cm^{-1}; this range is attributed to the stretching vibrations of oxygen-hydrogen groups. The band at the frequency of 1900 cm^{-1} is corresponded to the mixed vibrations, which do not contain information about the presence of oxygen-hydrogen groups or their state.

Table 1 Lattice parameters.

Compound	a, Å	c, Å
$Ba_5In_2Al_2ZrO_{13}$	5.967(2) [20]	24.006(8) [20]
$Ba_5In_2Al_2Zr_{0.9}In_{0.1}O_{12.95}$	5.970(1) [20]	24.011(4) [20]
$Ba_5In_2Al_2Zr_{0.9}Nb_{0.1}O_{13.05}$	5.966(1)	24.004(6)

Table 2 Elemental composition determined by the EDS for the $Ba_5In_2Al_2Zr_{0.9}Nb_{0.1}O_{13.05}$.

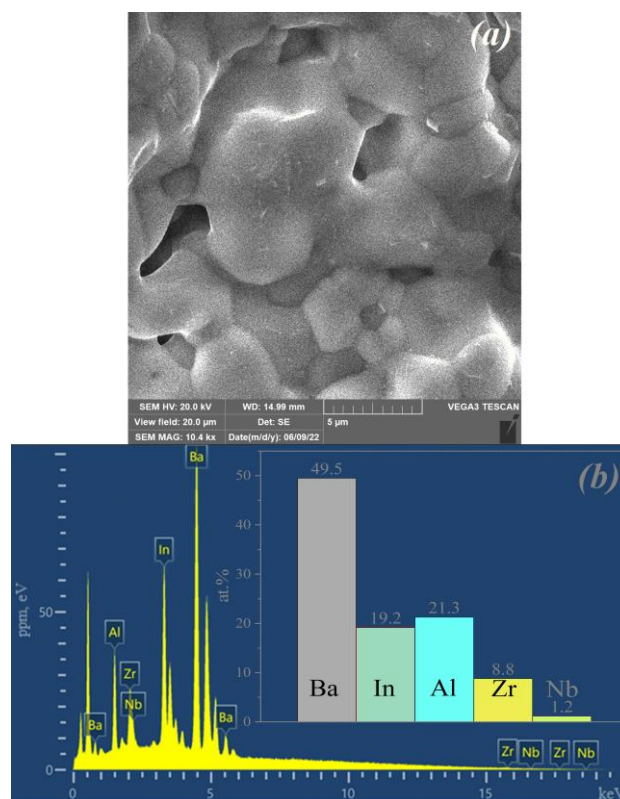| Theoretical values, at.%					EDS results, at.%				
Ba	In	Al	Zr	Nb	Ba	In	Al	Zr	Nb
50	20	20	9	1	49.5	19.2	21.3	8.8	1.2

Figure 2 SEM image for the ceramic sample of $Ba_5In_2Al_2Zr_{0.9}Nb_{0.1}O_{13.05}$ (a) and EDS results with the element fraction distribution histogram (at.%) for $Ba_5In_2Al_2Zr_{0.9}Nb_{0.1}O_{13.05}$ (b).

Figure 1 X-ray powder diffraction patterns for $Ba_5In_2Al_2ZrO_{13}$ (1) [20], $Ba_5In_2Al_2Zr_{0.9}In_{0.1}O_{12.95}$ (2) [20] and $Ba_5In_2Al_2Zr_{0.9}Nb_{0.1}O_{13.05}$ (3).

Identification of the oxygen-hydrogen groups state can be performed in terms of bending vibrations analysis. The presence of the band with the frequency ~1440 cm^{-1} indicates the existence of hydroxide OH$^-$ groups. The absence of bands at the frequencies ~1600 and 1700 cm^{-1} corresponds the absence of water molecules and hydroxonium ions H$_3$O$^+$, respectively. Therefore, the main form of oxygen-hydrogen groups present in hydrated samples is OH$^-$-group.

It can be seen that the wide band of stretching vibrations has a complex structure that indicates the presence of energetically nonequivalent OH$^-$-groups. Three overlapping bands can be distinguished. The main band maxima at ~3370 cm^{-1} and 3585 cm^{-1} show that some OH$^-$-groups should have a short length of the oxygen-hydrogen bond. Such hydroxide groups take part in weak hydrogen bonds. The lower maximum is located at ~2830 cm^{-1} and indicates the presence of OH$^-$-groups with a larger length of the O−H bond that are involved in strong hydrogen bonds. Thus, both substitution of zirconium by indium and niobium does not affect the oxygen-hydrogen groups state. Thus, we can conclude that at least three types of OH$^-$-groups are present in the structure, participating in different hydrogen bonds.

3.3. TG measurements

TG curves for Ba$_5$In$_2$Al$_2$ZrO$_{13}$, Ba$_5$In$_2$Al$_2$Zr$_{0.9}$In$_{0.1}$O$_{12.95}$ and Ba$_5$In$_2$Al$_2$Zr$_{0.9}$Nb$_{0.1}$O$_{13.05}$ are shown in Figure 4a. For convenience, the experimental data are presented as temperature dependence of degree of hydration x(H$_2$O), where x(H$_2$O) is the number of water molecules per formula unit. Generally, all the investigated samples demonstrate similar behavior: sufficiently monotonic mass changes with temperature. The mass changes were observed over a wide temperature range of 200–950 °C and at the temperatures above 950 °C mass stabilization occurred.
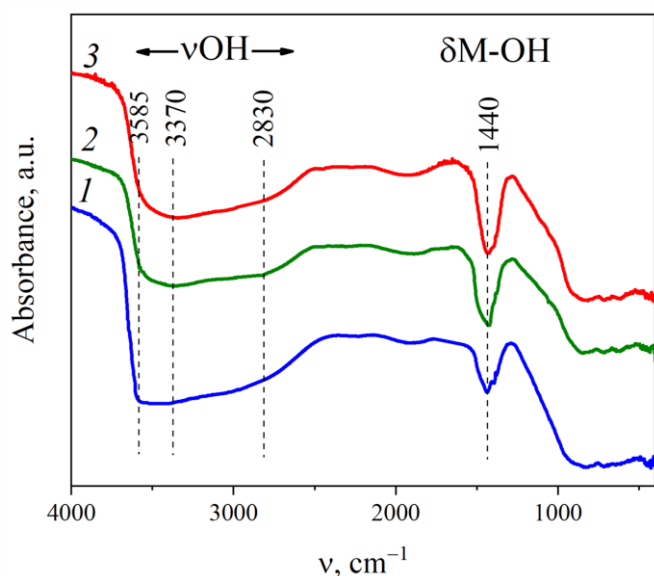
Figure 3 IR spectra of the hydrated samples of Ba$_5$In$_2$Al$_2$ZrO$_{13}$ (1) [20], Ba$_5$In$_2$Al$_2$Zr$_{0.9}$In$_{0.1}$O$_{12.95}$ (2) [20] and Ba$_5$In$_2$Al$_2$Zr$_{0.9}$Nb$_{0.1}$O$_{13.05}$ (3).

An ability of water incorporation from gas phase in the perovskite-related oxide is due to the presence of oxygen vacancies in their structure [24]. The structure of the parent compound Ba$_5$In$_2$Al$_2$ZrO$_{13}$ is represented as an intergrowth of two blocks of oxygen-deficient phase Ba$_2$InAlO$_5$ and one block of oxygen-stoichiometric perovskite BaZrO$_3$ [21]. Thereby, the investigated doped compound should have a potential ability of water incorporation that can be described by the following equation:

$$V_O^x + 2O_O^x + H_2O \rightleftarrows 2(OH)_O^\bullet + O''_{V_O^x}, \qquad (2)$$

where V_O^x is a structural oxygen vacancy, $(OH)_O^\bullet$ is a hydroxyl group on the oxygen site, $O''_{V_O^x}$ is the oxygen atom in the structural oxygen vacancy position.

For the phase Ba$_5$In$_2$Al$_2$Zr$_{0.9}$Nb$_{0.1}$O$_{13.05}$ the degree of hydration is x(H$_2$O) = 0.24 mol per mol of oxide. This value is lower in comparison with the degree of hydration for the undoped compound (x(H$_2$O) = 0.30 mol) and for the In^{3+}-doped phase (x(H$_2$O) = 0.41 mol). It can be explained by lower concentration of oxygen vacancies in the Nb^{5+}-doped compound. The process of donor doping by niobium (V) oxide was shown in equation 1; however, it can be rewritten by combining equation 1 and an equation that demonstrates filling an oxygen vacancy by an oxygen atom:
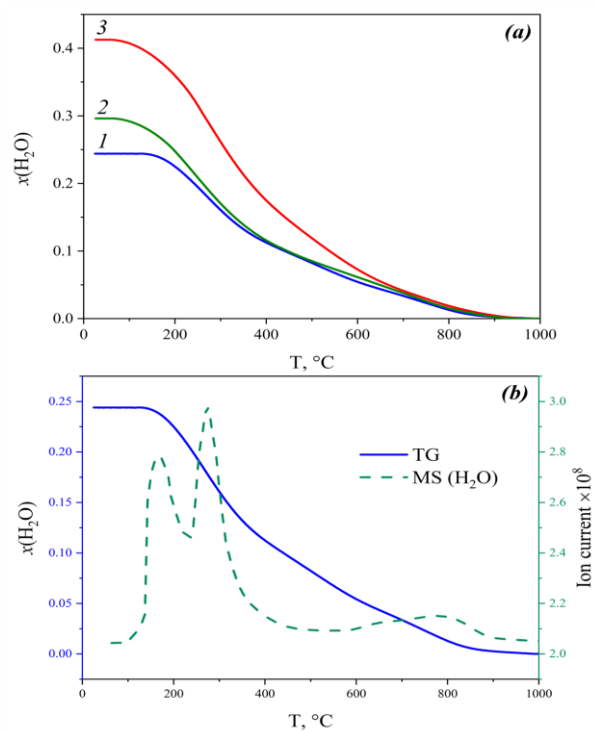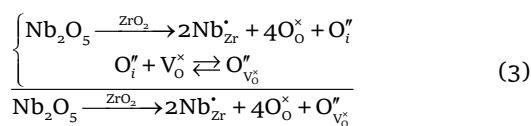
$$\begin{cases} Nb_2O_5 \xrightarrow{ZrO_2} 2Nb_{Zr}^\bullet + 4O_O^x + O''_i \\ O''_i + V_O^x \rightleftarrows O''_{V_O^x} \end{cases}$$
$$\overline{Nb_2O_5 \xrightarrow{ZrO_2} 2Nb_{Zr}^\bullet + 4O_O^x + O''_{V_O^x}} \qquad (3)$$

Figure 4 Temperature dependence of the hydration degree of Ba$_5$In$_2$Al$_2$Zr$_{0.9}$Nb$_{0.1}$O$_{13.05}$ (1), Ba$_5$In$_2$Al$_2$ZrO$_{13}$ (2) [20] and Ba$_5$In$_2$Al$_2$Zr$_{0.9}$In$_{0.1}$O$_{12.95}$ (3) [20] (pH$_2$O = 1.92·10^{-2} atm) (a); TG and MS curves for Ba$_5$In$_2$Al$_2$Zr$_{0.9}$Nb$_{0.1}$O$_{13.05}$ (b).

Thus, interstitial oxygen formed by substitution of zirconium by niobium can fill structural oxygen vacancies and make them incapable for water molecules incorporation; thereby, degree of hydration decreases. This case is opposite to the In^{3+}-doped compound, where substitution of zirconium by indium lead to the formation of the additional oxygen vacancies, which can be described by the equation:

$$In_2O_3 \xrightarrow{ZrO_2} 2In'_{Zr} + 3O^x_O + V^{\bullet\bullet}_O \,, \qquad (4)$$
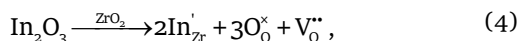
where In'_{Zr} represents In^{3+}-cation at a tetravalent Zr-site and $V^{\bullet\bullet}_O$ represents a charged oxygen vacancy. This explains the higher values of hydration degree of the In^{3+}-doped compound in comparison with the undoped compound.

According to IR-data the presence of different OH^--groups was established. As usual, this results in their different thermal stability, which is manifested on the TG-curves as the effects of mass changes in different temperature ranges. Although the TG-curve does not show pronounced steps of weight loss, the MS-spectrum demonstrates three effects of water release (Figure 4b). Thus, we can conclude that the data of IR spectroscopy and thermogravimetry are in good agreement with each other.

3.4. Transport properties

Figure 5 shows the typical impedance spectra for the $Ba_5In_2Al_2Zr_{0.9}Nb_{0.1}O_{13.05}$ in dry atmosphere at different temperatures (a) and at 343 °C in dry and wet atmospheres in comparison. It is seen that the temperature or water partial pressure changing does not affect the shape of spectra – impedance plots were similar in different conditions; with increasing humidity, the resistance of the sample significantly decreased. The presence of at least two relaxation processes can be found on impedance spectra: there are two overlapping semicircles in the main frequency range. Furthermore, the presence of the third relaxation process can be indicated in the region of low frequencies – there is a small part of the third semicircle; however, the contribution of this process in negligible. It is known that in polycrystalline samples relaxation processes can be connected with three contributions: bulk resistance of the material, resistance of the grain boundaries and the electrode surface processes [25].

The nature of these processes can be defined by analysis of the electrical capacitance values [26]. The capacitance values attributed to the third arc were about $\sim 10^{-6}$ F that is typical of the processes at the interface between ceramic samples and electrodes. The calculated capacitance values for the first and second arcs were about $\sim 10^{-11}$ and $\sim 10^{-10}$ F, respectively. It can be concluded that the first arc is attributed to the contribution of the bulk resistance and the second arc to the contribution of the grain boundaries resistance. It is worth to remark that the second semicircle is much smaller in comparison with the

first; thus, its contribution to the total resistance value should be insignificant. Thereby, for further discussions only bulk resistance values are used.

The values of electric conductivity were calculated according to the following equation:

$$\sigma = \frac{l}{SR_b} \,, \qquad (5)$$

where l is the sample thickness, S is the sample sectional area and R_b is the value of bulk resistance. Temperature dependences of the electric conductivity for $Ba_5In_2Al_2Zr_{0.9}Nb_{0.1}O_{13.05}$ in dry and wet air are presented in Figure 6a. It is seen that over the whole temperatures range the conductivity values obtained in wet air were higher in comparison with the dry air. With temperature decreasing the increase in the difference in conductivity values in wet and dry atmospheres were observed. It should be related to the hydration process which takes place in wet atmosphere; due to hydration, proton charge carriers are formed and the conductivity increases. At temperatures below 350 °C the difference in conductivity values obtained in different atmospheres becomes more than one order of magnitude. At 250 °C the difference reaches 1.5 orders. The difference between the values of conductivity in dry and wet air becomes insignificant at temperatures above 850 °C due to the dehydration process.
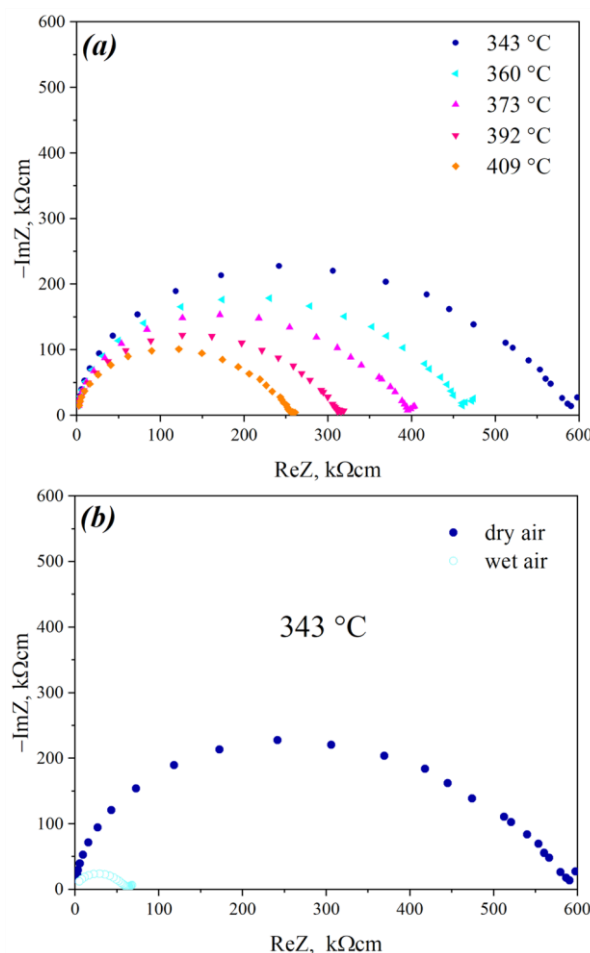

Figure 5 Impedance spectra for $Ba_5In_2Al_2Zr_{0.9}Nb_{0.1}O_{13.05}$ in dry air at different temperatures (a) and in dry and wet air at 343 °C (b).

Figure 6b demonstrates the temperature dependence of electric conductivity in wet atmosphere for $Ba_5In_2Al_2ZrO_{13}$, $Ba_5In_2Al_2Zr_{0.9}In_{0.1}O_{12.95}$ and $Ba_5In_2Al_2Zr_{0.9}Nb_{0.1}O_{13.05}$. It is seen, that conductivity values for $Ba_5In_2Al_2Zr_{0.9}Nb_{0.1}O_{13.05}$ are higher in comparison with those for the undoped and In^{3+}-doped compounds. At high temperatures the conductivity values for Nb^{5+}- and In^{3+}-doped phases are very close, while at low temperatures the electric conductivity of the Nb^{5+}-doped phase is lower than that for the In^{3+}-doped compound; at temperatures below 300 ºC the values of conductivity for $Ba_5In_2Al_2Zr_{0.9}Nb_{0.1}O_{13.05}$ are just slightly higher in comparison with the undoped compound.

For the determination of partial conductivities, the measurements of conductivity in a wide range of oxygen partial pressure were performed.

Figure 7a demonstrates the dependences of electric conductivity as a function of oxygen partial pressure in dry atmosphere. Over the oxygen partial pressure range 10^{-4}–0.21 atm the values of conductivity increase with oxygen partial pressure increasing. It indicates the presence of p-type conductivity σ_h contribution to the value of total electric conductivity. In this range of oxygen partial pressures the phase incorporates the oxygen from the gas phase that leads to the formation of holes; this process can be expressed by the equation:

$$V_O^{\times} + \frac{1}{2}O_2 \rightleftarrows 2h^{\bullet} + O''_{V_O^{\times}}, \qquad (6)$$
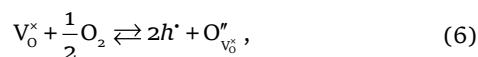
where $h^{\bullet}$ is the hole. In the oxygen partial pressure range 10^{-18}–10^{-4} atm the plateau was observed. This region is characterized by ionic defects domination; concentrations of electron defects in this oxygen partial pressure range are negligible. The plateau of ionic conductivity is attributed to the intrinsic oxygen vacancies $V_O^{\times}$ located in Ba_2InAlO_5 structural blocks. General view of the dependences does not change at different temperatures, though with temperature decreasing a slight decrease in the positive slope of the dependences can be observed. Thus, in air (0.21 atm) the total conductivity of the investigated compound can be characterized as a mixed oxygen-ion-hole conductivity.

Figure 7b shows the oxygen partial pressure dependences of total conductivity in dry and wet atmosphere in comparison. It is seen that over the whole oxygen partial pressure range the values of electric conductivity in wet atmosphere were higher than in dry atmosphere. The increase of the conductivity values in wet atmosphere is connected with the contribution of proton conductivity. With decreasing temperature, the difference in conductivity values in dry and wet atmospheres increase due to the hydration process and the increase in proton concentration. It should be noted that the difference between the values in dry and wet atmospheres increases with the decrease in the oxygen partial pressure. At 800 ºC in air the difference in the conductivity values is about 0.1 order of magnitude, while in the plateau region the difference rises to 0.4 orders of magnitude; at 600 ºC in the plateau region the difference between the conductivities in wet and

dry atmospheres is about 0.7 orders of magnitude. To conclude, the investigated compound can be characterized by the dominant ionic type of conductivity in the whole investigated range of oxygen partial pressures at temperatures below 600 ºC, and in air electric conductivity is mainly determined by the proton transport.

Oxygen partial pressure dependences of electric conductivity for $Ba_5In_2Al_2ZrO_{13}$ [20], $Ba_5In_2Al_2Zr_{0.9}In_{0.1}O_{12.95}$ [20], $Ba_5In_2Al_2Zr_{0.9}Nb_{0.1}O_{13.05}$ in dry and wet atmospheres in comparison are shown in Figure 8. The general view of the dependences for all the compounds is similar. In dry atmosphere the sample $Ba_5In_2Al_2Zr_{0.9}Nb_{0.1}O_{13.05}$ demonstrates a little lower positive slope on the conductivity dependence in the oxygen partial pressure range 10^{-4}–0.21 atm.

In wet atmosphere, conductivity values of $Ba_5In_2Al_2Zr_{0.9}Nb_{0.1}O_{13.05}$ are just a bit lower in comparison with $Ba_5In_2Al_2Zr_{0.9}In_{0.1}O_{12.95}$. The values of conductivity for $Ba_5In_2Al_2Zr_{0.9}Nb_{0.1}O_{13.05}$ are higher in comparison those in the with undoped compound over the whole oxygen partial pressure range in both dry and wet atmospheres.

The higher values of conductivity in wet atmosphere for the In^{3+}-doped phase in comparison with the Nb^{5+}-doped compound is due to additional oxygen vacancies in $Ba_5In_2Al_2Zr_{0.9}In_{0.1}O_{12.95}$ which were formed by acceptor doping; they incorporate water molecules according to the equation:
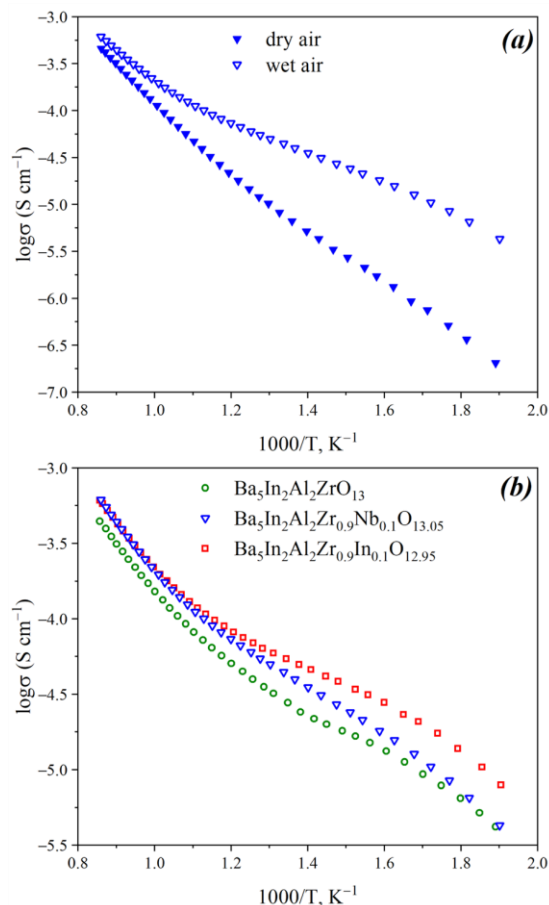
$$H_2O + V_O^{\bullet\bullet} + O_O^{\times} \rightleftarrows 2(OH)_O^{\bullet} \qquad (7)$$

Figure 6 Impedance spectra for $Ba_5In_2Al_2Zr_{0.9}Nb_{0.1}O_{13.05}$ in dry air at different temperatures (a) and in dry and wet air at 343 ºC (b).
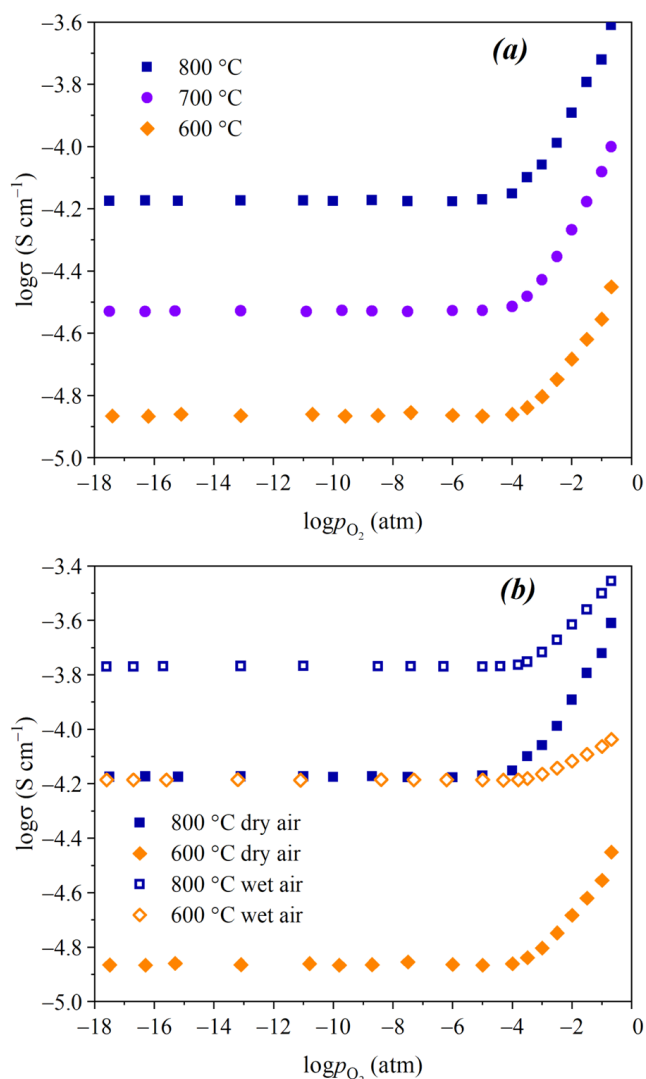
Figure 7 Oxygen partial pressure dependence of electric conductivity for $Ba_5In_2Al_2Zr_{0.9}Nb_{0.1}O_{13.05}$ in dry ($pH_2O = 3.5 \cdot 10^{-5}$ atm) atmosphere (a) and in dry and wet ($pH_2O = 1.92 \cdot 10^{-2}$ atm) atmospheres in comparison (b).
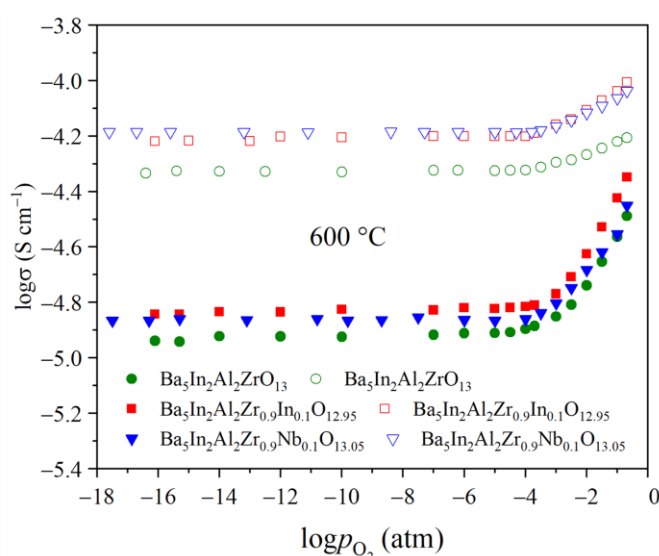

Figure 8 Oxygen partial pressure dependence of electric conductivity for $Ba_5In_2Al_2ZrO_{13}$ [20], $Ba_5In_2Al_2Zr_{0.9}In_{0.1}O_{12.95}$ [20], $Ba_5In_2Al_2Zr_{0.9}Nb_{0.1}O_{13.05}$ at 600 °C in dry ($pH_2O = 3.5 \cdot 10^{-5}$ atm) and wet ($pH_2O = 1.92 \cdot 10^{-2}$ atm) atmospheres in comparison (closed symbols are attributed to dry atmosphere, open symbols – to wet atmosphere).

Oxygen-ion and proton conductivities and transport numbers in air were calculated according to the data of conductivity dependence of oxygen partial pressure. Oxygen-ion conductivity $\sigma_{O^{2-}}$ was determined as conductivity values at the plateau region in dry atmosphere ($\sigma_{O^{2-}} = \sigma_{plateau}^{dry}$). Proton conductivity σ_H values were obtained by subtraction of ion conductivity in dry atmosphere (plateau region) from ion conductivity in wet atmosphere (plateau region, $\sigma_H = \sigma_{plateau}^{wet} - \sigma_{plateau}^{dry}$). Transport numbers t_i were calculated according to the following equation:

$$t_i = \frac{\sigma_i}{\sigma_{tot}}, \qquad (8)$$

where σ_i is the partial conductivity and σ_{tot} is the total conductivity in dry or wet air.

The temperature dependences of oxygen-ion conductivities are shown in Figure 9a. It is seen that the values of oxygen-ion conductivity are quite similar for the undoped compound and solid solutions based on it. The conductivity values for In^{3+}-doped compound are higher than those for the Nb^{5+}-doped one due to additional oxygen vacancies. The values of oxygen-ion conductivity for $Ba_5In_2Al_2Zr_{0.9}Nb_{0.1}O_{13.05}$ are comparable with those for the undoped compound. Thereby, substitution of zirconium by niobium does not affect significantly the oxygen-ion conductivity.

The oxygen-ion transport numbers dependences are presented in Figure 9b. In general, the transport numbers of all studied phases are close. Slightly lower values of oxygen-ion transport numbers for $Ba_5In_2Al_2Zr_{0.9}Nb_{0.1}O_{13.05}$ in comparison with those in the undoped and In^{3+}-doped compounds is due to lower oxygen vacancies concentrations. Thus, in dry air at low temperatures the Nb^{5+}-doped compound is a mixed oxygen-ion-hole conductors like the pure and In^{3+}-doped compounds.

Figure 10a shows the temperature dependences of proton conductivity. Over the whole investigated temperature range, the values of proton conductivity for $Ba_5In_2Al_2Zr_{0.9}Nb_{0.1}O_{13.05}$ were higher in comparison with those for the pure and In-doped compounds. Difference in values increases with temperature increasing, and at 800 °C the proton conductivity for Nb^{5+}-doped compound is higher in comparison with that for the pure phase by more than 0.3 orders of magnitude.

The temperature dependence of proton transport numbers is presented in Figure 10b. It is evident that the values of proton transport numbers for $Ba_5In_2Al_2Zr_{0.9}Nb_{0.1}O_{13.05}$ are higher than for $Ba_5In_2Al_2ZrO_{13}$ and $Ba_5In_2Al_2Zr_{0.9}In_{0.1}O_{12.95}$ in the whole investigated temperature range. With temperature decrease, the values of proton transport numbers rise because of the hydration process, and at temperatures below 600 °C in wet air for all the compounds the main contribution to the conductivity values is attributed to proton transport. Higher proton conductivity values for $Ba_5In_2Al_2Zr_{0.9}Nb_{0.1}O_{13.05}$ may be connected with electrostatic interactions between defects [27].

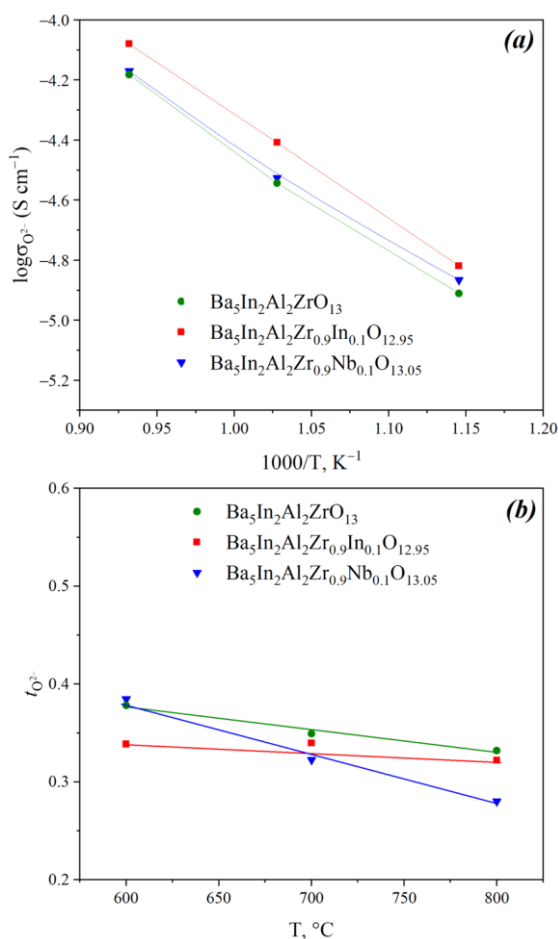**Figure 9** Temperature dependences of oxygen-ion conductivity (a) and oxygen-ion transport numbers (b) for $Ba_5In_2Al_2ZrO_{13}$ [20], $Ba_5In_2Al_2Zr_{0.9}In_{0.1}O_{12.95}$ [20] and $Ba_5In_2Al_2Zr_{0.9}Nb_{0.1}O_{13.05}$.

Figure 10 Temperature dependences of proton conductivity (a) and proton transport numbers (b) for $Ba_5In_2Al_2ZrO_{13}$ [20], $Ba_5In_2Al_2Zr_{0.9}In_{0.1}O_{12.95}$ [20] and $Ba_5In_2Al_2Zr_{0.9}Nb_{0.1}O_{13.05}$ (pH_2O = 1.92·10^{-2} atm).

As it was shown above in quasi-chemical modeling, substitution of zirconium by niobium leads to the formation of positively charged defects $Nb_{Zr}^{\bullet}$ in the zirconium sublattice. At the same time, water incorporation leads to the formation of proton defects $(OH)_O^{\bullet}$, which are also charged positively. Thereby, due to repulsion between positive charged defects, the mobility of protons increases.

To conclude, it should be said that phases based on the hexagonal perovskite $Ba_5In_2Al_2ZrO_{13}$ are promising proton conductors. This work showed that donor and acceptor doping is an advanced way for transport properties optimization.

4. Conclusions

The hexagonal perovskite $Ba_5In_2Al_2Zr_{0.9}Nb_{0.1}O_{13.05}$ was obtained through the solid state route. Substitution of zirconium by niobium led to the lattice parameters decrease in comparison with the parent compound.

TG measurements showed that the investigated compound is able to incorporate water. Due to lower concentration of oxygen vacancies Nb^{5+}-doped phase exhibited lower concentration of protons than the undoped phase; the hydration degree value for $Ba_5In_2Al_2Zr_{0.9}Nb_{0.1}O_{13.05}$ was $x(H_2O)$ = 0.24 mol. IR-spectroscopy analysis revealed the presence of OH^--groups with different thermal stability, which participate in different hydrogen bonds.
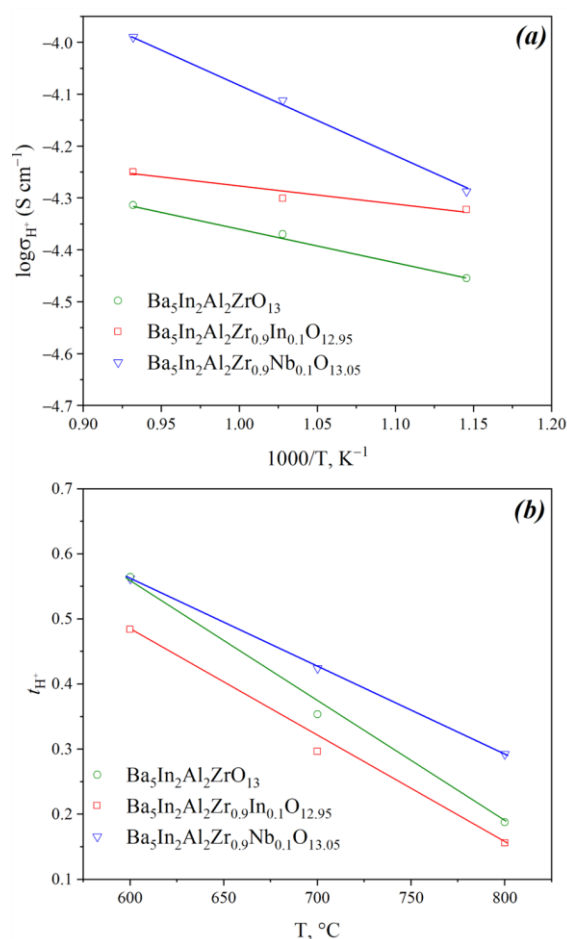
Electric properties measurements showed that $Ba_5In_2Al_2Zr_{0.9}Nb_{0.1}O_{13.05}$ is able to conduct protons in atmospheres with high water partial pressures. In dry air the phase is a mixed oxygen-ion-hole conductor, while in wet air below 600 °C $Ba_5In_2Al_2Zr_{0.9}Nb_{0.1}O_{13.05}$ exhibits dominating proton conductivity.

Supplementary materials

This manuscript contains supplementary materials, which are available on a corresponding online page.

Funding

Acknowledgments

None.

Author contributions

Conceptualization: I.E.A

Methodology: I.E.A, R.D.A.

X-ray diffraction analysis: I.A.A.

TG measurements: D.V.K.

SEM analysis: R.D.A.

IR analysis: R.D.A.

Conductivity measurements: R.D.A.

Writing – original draft: R.D.A., I.E.A.

Writing – review & editing: R.D.A., I.E.A.

Conflict of interest

The authors declare no conflict of interest.

Additional information

Author IDs:

　Roman D. Andreev, Scopus ID 57737857400;

　Daniil V. Korona, Scopus ID 13406057200;

　Irina A. Anokhina, Scopus ID 57219003831;

　Irina E. Animitsa, Scopus ID 6603520951.

Websites:

　Ural Federal University, https://urfu.ru/en;

　Institute of High Temperature Electrochemistry, http://www.ihte.uran.ru/?page_id=3106.

References

1. Malavasi L, Fisher CAJ, Islam MS. Oxide-ion and proton conducting electrolyte materials for clean energy applications: structural and mechanistic features. Chem Soc Rev. 2010;39:4370–4387. doi:10.1039/B915141A

2. Mengfei Z, Georgina J, Peimiao Z, Rong L, Mingtai W, Huanting W, Shanwen T. Recent development of perovskite oxide-based electrocatalysts and their applications in low to intermediate temperature electrochemical devices. Mater Today. 2021;49:351–377. doi:10.1016/j.mattod.2021.05.004

3. Mauro C, Maths K, Lorenzo M. Structure–property correlation in oxide-ion and proton conductors for clean energy applications: recent experimental and computational advancements. J Mater Chem A. 2022;10:5082–5110. doi:10.1039/d1ta10326a

4. Ashish K, Ajay K, Venkata K. Perovskite oxide based materials for energy and environment- oriented photocatalysis. ACS Catal. 2020;10(17):10253–10315. doi:10.1021/acscatal.0c02947

5. Tatsumi I. Inorganic perovskite oxides. Springer Handbook of Electronic and Photonic Materials. Springer International Publishing: Germany; 2017. 1572 p.

6. Wan-Jian Y, Baicheng W, Jie G, Qingde S, Zhenzhu L, Yanfa Y. Oxide perovskites, double perovskites and derivatives for electrocatalysis, photocatalysis, and photovoltaics. Energy Environ Sci. 2019;12:442–462. doi:10.1039/c8ee01574k

7. Medvedev D. Trends in research and development of protonic ceramic electrolysis cells. Int J Hydrog Energy. 2019;44:26711–26740. doi:10.1016/j.ijhydene.2019.08.130

8. King G, Woodward PMJ. Cation ordering in perovskites. Mater Chem. 2010;20:5785–5796. doi:10.1039/B926757C

9. Animitsa I. Double perovskites with structure-disordered oxygen sublattice as high-temperature proton conductors. In Perovskites: Structure, Properties and Uses. Nova Science Publishers, Inc.: USA; 2010. p. 501–524.

10. Murugaraj P, Kreuer K, He T, Schober T, Maier J. High proton conductivity in barium yttrium stannate $Ba_2YSnO_{5.5}$. Solid State Ion. 1997;98:1–6. doi:10.1016/S0167-2738(97)00102-1

11. Baliteau S, Mauvy F, Fourcade S, Grenier J. Investigation on double perovskite $Ba_4Ca_2Ta_2O_{11}$. Solid State Sci. 2009;11:1572–1575. doi:10.1016/j.solidstatesciences.2009.06.023

12. Jalarvo N, Haavik C, Kongshaug C, Norby P, Norby T. Conductivity and water uptake of $Sr_4(Sr_2Nb_2)O_{11} \cdot nH_2O$ and $Sr_4(Sr_2Ta_2)O_{11} \cdot nH_2O$. Solid State Ion. 2009;180:1151–1156. doi:10.1016/j.ssi.2009.05.021

13. Gurudeo N, Dharmendra Y, Shail U. Ruddlesden–Popper phase A_2BO_4 oxides: Recent studies on structure, electrical, dielectric, and optical properties. J Adv Ceram. 2020;9(2):29–148. doi:10.1007/s40145-020-0365-x

14. Hayden AE, Lingling M, Ram S, Anthony KC. Layered double perovskites. Annu Rev Mater Res. 2021;51:1–33. doi:10.1146/annurev-matsci-092320-102133

15. Armstrong AR, Anderson PA. Synthesis and structure of a new layered niobium blue bronze: $Rb_2LaNb_2O_7$. Inorg Chem. 1994;33(19):4366–4369. doi:10.1021/ic00097a026

16. Le Berre F, Crosnier-Lopez MP, Fourque, JL. Cationic ordering in the new layered perovskite $BaSrTa_2O_7$. Solid State Sci. 2004;6(1):53–59. doi:10.1016/j.solidstatesciences.2003.10.008

17. Fop S, McCombie K, Wildman E, Skakle J, Irvine J, Connor P, Savaniu C, Ritter C, Mclaughlin A. High oxide ion and proton conductivity in a disordered hexagonal perovskite. Nat Mater. 2020;19:752–757. doi:10.1038/s41563-020-0629-4

18. Fop S, Dawson J, Fortes A, Ritter C, McLaughlin A. Hydration and ionic conduction mechanisms of hexagonal perovskite derivatives. Chem Mater. 2021;33:4651–4660. doi:10.1021/acs.chemmater.1c01141

19. Murakami T, Hester J, Yashima M. High proton conductivity in $Ba_5Er_2Al_2ZrO_{13}$, a hexagonal perovskite-related oxide with intrinsically oxygen-deficient layers. J Am Chem Soc. 2020;142:11653–11657. doi:10.1021/jacs.0c02403

20. Andreev R, Korona D, Anokhina I, Animitsa I. Proton and oxygen-ion conductivities of hexagonal perovskite $Ba_5In_2Al_2ZrO_{13}$. Mater. 2022;15(11):3944. doi:10.3390/ma15113944

21. Shpanchenko R, Abakumov A, Antipov E, Kovba L. Crystal structure of $Ba_5In_2Al_2ZrO_{13}$. J Alloy Compd. 1994;206:185–188. doi:10.1016/0925-8388(94)90033-7

22. Yashima M, Tsujiguchi T, Sakuda Y, Yasui Y, Zhou Y, Fujii K, Torii Sh, Kamiyama T, Skinner SJ. High oxide-ion conductivity through the interstitial oxygen site in $Ba_7Nb_4MoO_{20}$-based hexagonal perovskite related oxides. Nat Commun. 2021;12(1):1–7. doi:10.1038/s41467-020-20859-w

23. Shannon R. Revised effective ionic radii and systematic studies of interatomic distances in halides and chalcogenides. Acta Crystallogr Sect A Cryst Phys Diffr Theor Gen Crystallogr. 1976;32:751–767. doi:10.1107/S0567739476001551

24. Stotz S, Wagner C. Die Loslichkeit von Wasserdampf und Wasserstoff in Festen Oxiden. Ber Bunsenges Phys Chem. 1967;70(8):781–788. doi:10.1002/bbpc.19660700804

25. Lasia A. Electrochemical Impedance Spectroscopy and Its Applications. Modern Aspects of Electrochemistry. Springer: New York, USA; 2014. p. 143–258.

26. Irvine J, Sinclair D, West A. Electroceramics: Characterization by Impedance Spectroscopy. Adv Mater. 1990;2:132–138. doi:10.1002/adma.19900020304

27. Tarasova N, Animitsa I. Anionic doping (F^-, Cl^-) as the method for improving transport properties of proton-conducting perovskites based on $Ba_2CaNbO_{5.5}$. Solid State Ion. 2018;317:21–25. doi:10.1016/j.ssi.2018.01.001